

COORDINATE-BASED NEURAL NETWORK FOR FOURIER PHASE RETRIEVAL

Tingyou Li^{1,*}, Zixin Xu^{1,*}, Yong S. Chu², Xiaojing Huang², Jizhou Li¹

¹School of Data Science, City University of Hong Kong, Hong Kong SAR

²National Synchrotron Light Source II, Brookhaven National Laboratory, USA

ABSTRACT

Fourier phase retrieval is essential for high-definition imaging of nanoscale structures across diverse fields, notably coherent diffraction imaging. This study presents the Single impliCit neural Network (SCAN), a tool built upon coordinate neural networks meticulously designed for enhanced phase retrieval performance. Remedying the drawbacks of conventional iterative methods which are easily trapped into local minimum solutions and sensitive to noise, SCAN adeptly connects object coordinates to their amplitude and phase within a unified network in an unsupervised manner. While many existing methods primarily use Fourier magnitude in their loss function, our approach incorporates both the predicted magnitude and phase, enhancing retrieval accuracy. Comprehensive tests validate SCAN's superiority over traditional and other deep learning models regarding accuracy and noise robustness. We also demonstrate that SCAN excels in the ptychography setting.

Index Terms— Fourier phase retrieval, implicit neural representation, coordinate-based neural network, coherent diffraction imaging, ptychography

1. INTRODUCTION

In imaging systems, detectors typically capture only the amplitude of incoming light, leaving the phase information unrecorded. This omission gives rise to the Fourier phase retrieval challenge, wherein the objective is to reconstruct the lost phase information from the recorded amplitude. Typical applications of Fourier phase retrieval include X-ray crystallography and coherent diffraction imaging (CDI). Successfully retrieving the phase can lead to high-resolution, detailed images of subjects down to the atomic level. In general, Fourier phase retrieval aims to use the measured Fourier magnitude to recover the original object and can be formally written as

$$\mathcal{F}(k) = |\mathcal{F}(k)|e^{i\psi(k)} = \int_{-\infty}^{\infty} f(x)e^{-2\pi i k x} dx, \quad (1)$$

where x is an n -dimensional spatial coordinate, and k is an n -dimensional spatial frequency coordinate. $|\mathcal{F}(k)|$ is what we measured on the detector while $\psi(k)$ is lost and needs to be recovered. The $f(x)$ and $|\mathcal{F}(k)|$ in the above formulation could have different meanings in different applications. For example, in the transmission mode of CDI, the reconstructed amplitude and phase in $f(x)$ represent the imaginary and real parts of the sample's refractive index; in the Bragg diffraction mode, its magnitude represents the electron density, and phase denotes the projection of the local deformations of the crystal lattice onto the reciprocal lattice vector Q of the Bragg peak about which the diffraction is measured [1].

* Equal contribution. This work is supported by City University of Hong Kong under grant 9610619.

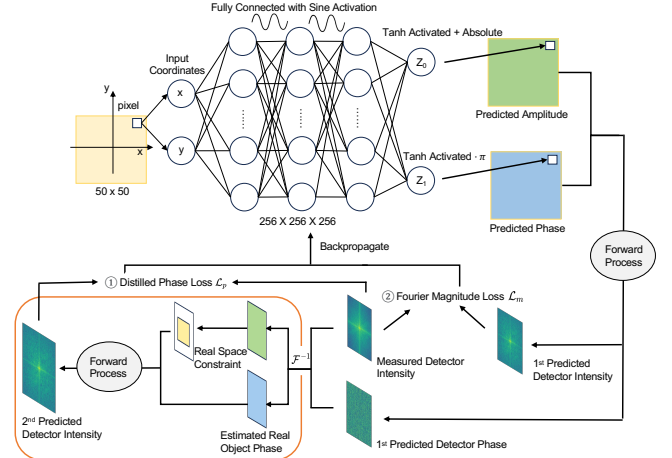


Fig. 1: Illustration of the proposed SCAN approach for Fourier phase retrieval.

Despite its critical importance across various domains, the Fourier phase retrieval often remains an elusive challenge due to issues like insufficient oversampling [2, 3]. Further complications arise from global phase shifts, shift symmetries, and flip symmetries [4], making it an inherently complex non-convex problem. Addressing these challenges, traditional alternating projection techniques like Gerchberg–Saxton (GS) [5] and Error Reduction (ER) [6] alternate between real and Fourier spaces, enforcing known constraints on their results. However, local optima frequently ensnare these approaches, resulting in sluggish convergence. To mitigate this, methods like HIO [6, 7] have eased these constraints, widening the range of feasible solutions to achieve enhanced performance. Yet, empirical studies indicate that these iterative methods remain susceptible to disruptions from noise [8]. Consequently, they often necessitate extensive iterations and multiple random initializations to obtain reliable results [9].

There has been a growing interest in harnessing the capabilities of deep learning to address the limitations inherent in traditional phase retrieval methods. Supervised learning methods, exemplified by approaches like CDI NN [10], SiSPRNet [11] and others [12, 13], primarily employ encoder-decoder architectures in CNNs to transform input intensities into complex objects. A notable innovation in this arena is the work presented in [12], which artfully combines supervised learning with transfer learning techniques, refining results in a more adaptable manner. However, even with such advancements, these methods often come with challenges, requiring significant preparatory work and training and potentially faltering when faced with divergent data sets [8].

Recognizing the practical requirements, researchers have turned to unsupervised learning methodologies. A prevalent trend within this domain involves utilizing encoder-decoder CNNs, yet without

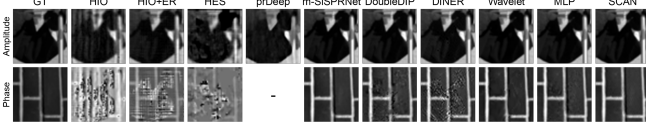


Fig. 2: Best performance of different methods under noise-free condition

the necessity for pre-training [3, 8, 14, 15, 16]. Concurrently, other strategies emerged, leveraging denoising models as a form of regularization [17], or introducing specific priors during the recovery process [18]. However, the current decoder-encoder-based CNN models may need to tune many parameters before applying them to new data. For example, the convolution stride, the channels, and the block number may need to be changed once the output size is changed. And it could be computationally inefficient once the block increases. Besides, most models [3, 14, 15, 16] only used Fourier magnitude for supervision during training while the predicted phase is not in use.

The intrinsic nature of objects, namely their coordinates, offers an accurate and compact representation. Each coordinate maps directly to its corresponding object amplitude and phase, forming the foundation of the Implicit Neural Representation (INR) concept, a paradigm that has recently been introduced to the research community [19, 20, 21]. Prior to our study, this framework demonstrated substantial success in image inversion tasks [19, 22, 23, 24, 25, 26]. For instance, NeRF [19] focuses on refining the object’s density and color based on multiple viewpoints from various angles. CoIL [24] trains a multilayer perceptron (MLP) to encode the complete measurement field and demonstrates superior performance in sparse-view computed tomography reconstruction. Notably, while DINER [27] and DNF [28] have successfully applied INR for phase recovery, a deeper dive reveals their objective is not Fourier phase retrieval. To our knowledge, there remains an unexplored potential for the INR framework tailored for Fourier phase retrieval. Our contributions can be summarized as follows:

- We design an unsupervised single coordinate-based neural network (SCAN) based on INR to predict object amplitude and phase simultaneously.
- We propose a novel loss function to guide the training phase of SCAN for improved performance.
- We benchmark our method against current state-of-the-art (SOTA) algorithms, underscoring its potential through quantitative measurements in CDI and Ptychography experiments.

2. METHODS

In CDI, the problem can be represented by

$$I(\mathbf{q}) = |\mathcal{F}\{O(\mathbf{r})\}|^2, \mathcal{F}\{O(\mathbf{r})\} \in \mathbb{C}^{\tilde{M} \times \tilde{N}}, O(\mathbf{r}) \in \mathbb{C}^{M \times N}, \quad (2)$$

where $\tilde{M} \geq 2M - 1$, $\tilde{N} \geq 2N - 1$ provide additional information for image recovery. In ptychography, a localized probe is scanned over an extended object, and a series of measurements are collected from overlapping positions:

$$I_j(\mathbf{q}) = |\mathcal{F}\{P(\mathbf{r} - \mathbf{r}_j) * O(\mathbf{r})\}|^2, \quad (3)$$

where $\mathcal{F}\{\cdot\}$ is the Fourier transform, $O(\mathbf{r})$ represents the object, $P(\mathbf{r} - \mathbf{r}_j)$ denotes the probe scanning the object at position j , \mathbf{r} and \mathbf{q} are the real space and the Fourier space coordinate. Our idea is to parameterize objects as a (continuous) function represented by $f_\theta(z)$, where z is a set of coordinates, and $f_\theta(\cdot)$ symbolizes a deep neural network with parameters θ . The following equations are formulated in the CDI context, with the ptychography variation conceptualized as scanning CDI employing $P(\mathbf{r} - \mathbf{r}_j)$.

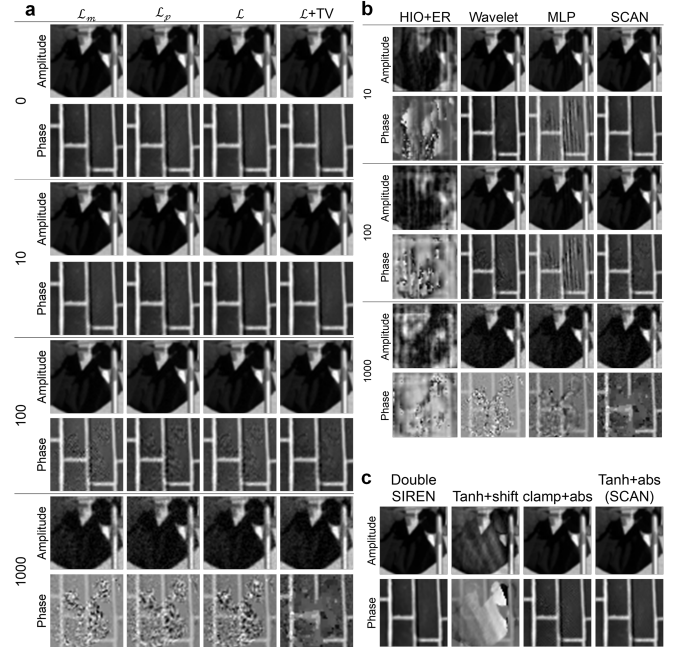


Fig. 3: (a) Ablation study of different loss functions under different noise levels ($\sigma = 0, 10, 100, \text{ and } 1000$); (b) comparison of noise robustness across different methods; (c) ablation study of network architectures.

The network architecture is illustrated in Fig. 1. The first part is about image coordination, which involves encoding pixels using spatial coordinates. Subsequently, image coordinates are used as inputs for a fully connected network featuring sine activation [20] to obtain simultaneously the predicted phase and amplitude. The network parameters are iteratively adjusted during training using a meticulously defined loss function; see the details in Sec. 2.3.

2.1. Image Coordination

The entire 2D image is categorized into four quadrants centered around the image’s midpoint. Each pixel’s horizontal and vertical coordinates are uniformly projected (or normalized) within the range $[-1, 1] \times c$, where c is found to be an influential hyperparameter that impacts both the final network outcome and the learning rate. This might be because varying coordinate scales affect the network’s initialization output. For smaller values of c , the last linear layer output is more homogeneous within a constricted range. Conversely, the output tends to be more normally distributed for larger values. Despite the choice of c , the ultimate performance of SCAN remains consistent across different weight initializations. Our experiments found c to be optimally set at 0.1.

2.2. Backbone of Main Network

The fully connected network consists of three hidden layers, each with 256 units, and a concluding output layer with two units. While hidden layers are integrated with sine activation adapted from SIREN [20], the final output layer is followed by a Tanh activation function in our approach. The primary output unit predicts the object’s amplitude, whereas the second determines its phase. Therefore, an absolute operation is performed after activating the first output unit. The second output is multiplied by π to ensure the phase range is scaled to $[-\pi, \pi]$. The process can be written as:

$$\widehat{O}(\mathbf{r}) = |f_{\theta_1}(z)| e^{i f_{\theta_2}(z) \pi}, \quad (4)$$

where z is coordinate normalization from \mathbf{r} and $f_{\theta_1}(z)$, $f_{\theta_2}(z)$ represent the outputs from the first and second channel, respectively.

	HIO	HIO+ER	HES	prDeep	m-SiSPRNet	Double DIP	DINER	Wavelet	MLP	SCAN
Amp	20.12 / 0.54	22.52 / 0.85	19.30 / 0.49	22.49 / 0.65	66.81 / 0.9999	45.84 / 0.99	35.18 / 0.90	53.31 / 0.998	46.26 / 0.99	55.46 / 0.999
Phase	8.12 / 0.17	12.94 / 0.32	11.74 / 0.26	-	37.46 / 0.997	26.95 / 0.83	23.08 / 0.68	27.84 / 0.92	36.43 / 0.94	45.30 / 0.99

Table 1: The best performance over three random seeds of different methods under noise-free conditions (PSNR / SSIM).

	HIO	HIO+ER	HES	prDeep	m-SiSPRNet	Double DIP	DINER	Wavelet	MLP	SCAN
Amp	13.79±6.89	18.52±5.01	17.48±4.68	18.50±4.25	29.82±26.46	21.43±17.05	24.81±7.70	52.72±0.75	36.88±17.25	63.06±5.40
Phase	9.02±1.08	11.52±2.67	10.09±1.18	-	21.10±11.57	16.01±7.74	14.72±5.91	25.13±1.95	23.90±10.86	42.43±2.43

Table 2: Stability of different methods in mean±std (PSNR).

It’s worth highlighting that SCAN utilizes just one fully connected network. This design choice means SCAN has a limited set of hyperparameters — specifically, the learning rate, layer size, and number of layers. In contrast, approaches with separate networks for amplitude and phase outputs often demand more intricate tuning, such as individualized learning rates and layer adjustments. As a result, SCAN benefits from having fewer parameters, streamlining the optimization process.

2.3. Loss Function

2.3.1 Fourier Magnitude Loss (\mathcal{L}_m). Upon forward propagation through the network, the predicted amplitude and phase undergo additional forwarding to derive the predicted Fourier magnitude and phase. The primary loss metric evaluates the discrepancy between the predicted Fourier magnitude and the actual measurements. This form of loss assessment is commonly employed in unsupervised end-to-end methodologies [3, 14, 15, 16] because it directly quantifies the accuracy of the Fourier magnitude prediction. We write it as:

$$\mathcal{L}_m = \left\| |\mathcal{F}\{\widehat{O}(\mathbf{r})\}| - \sqrt{I(\mathbf{q})} \right\|_2^2. \quad (5)$$

2.3.2 Distilled Fourier Phase Loss (\mathcal{L}_p). We further leverage the predicted phase by incorporating it into the loss calculation after suitable adjustments. Inspired by ER [7], which employs iterative processes between real and Fourier spaces, we integrate the predicted Fourier phase u with measured detector intensity I to transition back to the real space, as illustrated in Fig. 1. Subsequently, we apply recognized constraints in the real space, denoted by $\odot S$, to this transformed object. These constraints enforce that the padding area should be zero and the object amplitude must reside within the 0-1 range. After imposing these constraints on the transformed object, we transition it forward to the Fourier space, deriving the Fourier magnitude for the second time. The secondary loss evaluates the disparity between this second-time predicted Fourier magnitude and the actual measurement.

The underlying rationale for the second loss \mathcal{L}_p is that if the predicted Fourier phase is accurate, the merging of this phase with the true Fourier magnitude, coupled with the back-and-forth transitions between the Fourier and real spaces under established constraints, should yield a Fourier magnitude consistent with the measured one. The equations are detailed below. In this context, \widehat{O}_a and \widehat{O}_p represent the amplitude and the phase of the predicted object, respectively. They arise from the fusion of the measured detector intensity I and the predicted detector phase u .

$$u = \text{angle}(\mathcal{F}\{\widehat{O}(\mathbf{r})\}), \quad (6)$$

$$\widehat{O}_a = |\mathcal{F}^{-1}\{\sqrt{I}e^{iu}\}| \odot S, \quad \widehat{O}_p = \text{angle}(\mathcal{F}^{-1}\{\sqrt{I}e^{iu}\}), \quad (7)$$

$$\mathcal{L}_p = \left\| |\mathcal{F}\{\widehat{O}_a e^{i\widehat{O}_p}\}| - \sqrt{I} \right\|_2^2. \quad (8)$$

2.3.3 Final Loss Function. Our ultimate training loss constitutes a blend of these individual losses. Both losses \mathcal{L}_m and \mathcal{L}_p are deemed equally significant during training. However, given that their magnitudes differ, it’s necessary to preface each with an appropriate

weight. The cumulative loss is expressed as $\mathcal{L} = W_1 \times \mathcal{L}_m + W_2 \times \mathcal{L}_p$. In subsequent experiments, considering the initial ratio of Fourier magnitude loss to Distilled Fourier phase loss to be approximately 7:3, we set $W_1 = 0.3$ and $W_2 = 0.7$ for simplicity. Moreover, a Total Variation (TV) loss on the predicted phase is further incorporated for scenarios with noise disruption. By incorporating the TV loss, we promote smoother phase transitions and improve the overall quality of the phase predictions.

3. EXPERIMENTS

3.1. Experimental setup

Two commonly employed test images are utilized in our subsequent experiments: the *cameraman* and the *brick*. These images are resized to dimensions 256×256 and are normalized using min-max normalization to the range [0,1] prior to experimentation. We will evaluate the performance of the proposed SCAN method in comparison with state-of-the-art techniques in both the CDI and Ptychography settings. Analysis of our approach, including ablation studies, will also be conducted.

Coherent Diffraction Imaging (CDI). In the existing studies, the oversample rate for most experiments is typically set around 2, with the actual object positioned ambiguously within the designated area. Consequently, a shifted symmetry may be observed during the recovery phase, as noted in [4]. Moreover, areas outside the object could potentially register values due to the quality of recovery. This scenario complicates the adoption of quantitative quality metrics like PSNR or SSIM. While the shrinkwrap method [29], which reduces minor values to zero, might provide a solution, the threshold for shrinkwrap can significantly vary across experiments, rendering comparisons unfair. Hence, we set the known object size to match the unpadded area in subsequent experiments to circumvent the shift issue and concentrate solely on the model’s recovery capability. We chose an oversample rate of approximately 5 for all benchmarked methods. Our simulated 2D object amplitude is a segment of the cameraman image (50×50 pixels), and the object phase derives from a portion of the brick image of the same size (Fig. 2).

In our experimentation, we will compare traditional alternating projection techniques such as HIO, HIO+ER [7], and HES [29] as well as deep models like SiSPRNet [11], prDeep [17], and DINER [27]. Given that our model employs sine activation function, we also assessed other potential backbones for this task. The Deep Image Prior [30], MLP with a positional encoder, and a recent wavelet approach [21] are also examined. It’s worth mentioning that SiSPRNet [11] operates as a supervised model. For the purposes of this study, we only adapted its architectural structure (CNN-based decoder-encoder) for comparison, referring to it as m-SiSPRNet. Additionally, only the real recovery component in prDeep [17] is factored into our comparative analysis.

With the above settings, we are interested in the following aspects: (1) Recovery performance under noise-free conditions; (2) Stability of the models; (3) Noise robustness; (4) Ablation studies of our approach, such as the loss function, network architectures etc.

		HIO+ER	Wavelet	MLP	SCAN
10	Amp	16.14 / 0.36	52.83 / 0.998	32.99 / 0.71	61.13 / 0.999
	Phase	11.22 / 0.12	26.74 / 0.92	18.25 / 0.57	35.42 / 0.98
100	Amp	14.51 / 0.21	42.62 / 0.98	31.30 / 0.70	42.93 / 0.98
	Phase	9.21 / 0.09	26.48 / 0.84	18.81 / 0.55	26.42 / 0.85
1000	Amp	11.65 / 0.22	29.03 / 0.75	23.81 / 0.58	29.19 / 0.76
	Phase	8.22 / 0.09	9.74 / 0.25	10.61 / 0.28	17.18 / 0.58

Table 3: Performance of phase retrieval methods under noisy conditions (PSNR / SSIM)

Ptychography. Distinct from the CDI setting, the ptychography experiment aims to recover the whole image (256×256 pixels) with multiple measured intensities. It has a simulated probe with a dimension of 28×28 derived from [31] to scan different positions of the whole image. Since most existing networks are tailored for CDI, our model’s benchmark will be ePIE. Notably, the overlap rate plays a pivotal role in determining the quality of reconstruction and the computational time. Hence, we evaluate the model’s performance across different overlap rates, specifically at 30%, 50%, and 70%.

3.2. Model Training

We evaluated SCAN on a server with one NVIDIA GeForce RTX 3090 GPU. All models use Adam optimizer for training. Only the learning rate is changed in optimizer hyperparameters. For SCAN, the learning rate is fixed to be 0.8×10^{-4} . For other methods, learning rates are adjusted to obtain the best performance. The batch size is set to be 1 as it inputs the whole image for each epoch.

4. RESULTS

4.1. Results of CDI setting

Noise Free Condition. Under noise-free conditions, Tab. 1 and Fig. 2 show the best results for each method out of 3 random realizations (seeds). m-SiSPRNet achieved the best performance in amplitude recovery, followed by SCAN and wavelet. For object phase recovery, SCAN performed the best, then MLP and m-SiSPRNet. Phase is found to be harder than amplitude to recover. The same model could have quite different recovery abilities on these two properties. For instance, m-SiSPRNet’s phase recovery is 30 dB lower than its amplitude result. However, SCAN balanced the results and achieved good performance on both.

Stability. Tab. 2 shows the mean and standard deviation of 3 seeds’ experiment results under the noise-free condition. SCAN has the best amplitude and phase recovery performance when considering all seeds. It is noticed that decoder-encoder-based models, m-SiSPRNet and Double DIP, have a high variance in results. SCAN had a relatively lower variance, demonstrating its high stability.

Noise Robustness. Tab. 3 and Fig. 3(a) show the restoration performance under different noise levels. In most cases, SCAN outperforms all methods, especially in retrieving the object phase.

Ablation Study of Loss Function. As shown in Tab. 4 and Fig. 3(b), the \mathcal{L}_p recovers the phase better than \mathcal{L}_m in most cases. The model with the combination of these two losses improves the recovery quality of the phase compared with the one with \mathcal{L}_m , and the amplitude recovery outperforms both. The performance is further enhanced after adding a TV loss, mainly in the phase part.

Ablation Study of Different Model Structures. Tab. 5 and Fig. 3 present several potential model implementations. The terms “clamp” and “shift” are utilized to denote alternative approaches to the Tanh activation function and absolute operation, respectively. Specifically, “clamp” refers to constraining the value within the range of $[-1, 1]$, while “shift” involves scaling the value x to the range of $[0, 1]$ using the transformation $(x + 1)/2$. Additionally, we explored utilizing two separate networks, one for object amplitude and the other for

		\mathcal{L}_m	\mathcal{L}_p	\mathcal{L}	$\mathcal{L}+TV$
0	Amp	50.50 / 0.99	52.23 / 0.99	63.06 / 0.999	63.06 / 0.999
	Phase	32.88 / 0.93	36.63 / 0.94	42.43 / 0.99	42.43 / 0.999
10	Amp	53.97 / 0.996	52.81 / 0.998	59.78 / 0.999	61.13 / 0.999
	Phase	38.46 / 0.96	33.41 / 0.93	34.72 / 0.98	35.42 / 0.98
100	Amp	42.33 / 0.97	42.71 / 0.97	42.58 / 0.97	42.93 / 0.98
	Phase	19.01 / 0.74	23.60 / 0.80	21.48 / 0.79	26.42 / 0.85
1000	Amp	28.53 / 0.74	26.61 / 0.67	28.59 / 0.75	29.19 / 0.76
	Phase	10.35 / 0.27	10.18 / 0.30	11.10 / 0.32	17.18 / 0.58

Table 4: Ablation study of different loss function. (PSNR / SSIM)

	Double SIREN	Tanh+shift	clamp+abs	Tanh+abs (SCAN)
Amp	43.75 / 0.88	12.77 / 0.28	62.44 / 0.999	63.06 / 0.999
Phase	25.27 / 0.73	9.53 / 0.22	37.01 / 0.986	42.43 / 0.99
Time(s)	448.02	-	-	324.52

Table 5: Ablation study of different model structures. (PSNR / SSIM)

	30%			50%			70%		
	Amp	Phase	Time(s)	Amp	Phase	Time(s)	Amp	Phase	Time(s)
ePIE	9.75 / 0.20	11.03 / 0.20	76.58	10.08 / 0.17	11.14 / 0.23	141.10	29.70 / 0.90	17.72 / 0.80	394.69
SCAN	23.06 / 0.82	15.38 / 0.70	24.14	25.15 / 0.81	16.02 / 0.71	35.77	34.65 / 0.98	21.23 / 0.87	237.08

Table 6: Ptychography reconstruction of ePIE and SCAN when the overlap rate is 30%, 50%, and 70%. (PSNR / SSIM)

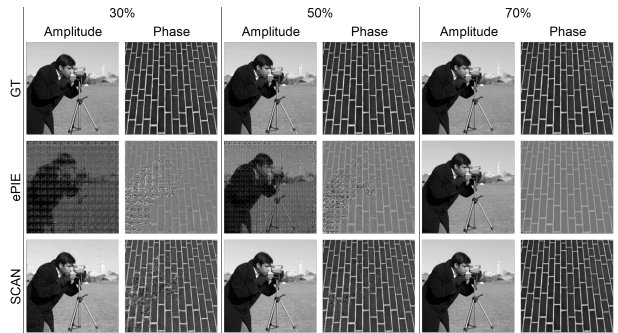


Fig. 4: Ptychographic reconstruction comparisons between ePIE and SCAN at overlap rates of 30%, 50%, and 70%.

phase representation. The results demonstrate that our current implementation in SCAN outperforms all other approaches.

4.2. Results of Ptychography setting

As shown in Tab. 6 and Fig. 4, SCAN exhibits superior quality in reconstructions at low overlap rates of 30% and 50%. In contrast, ePIE necessitates an overlap in the range of 70% to achieve commendable results, as referenced in [32]. Notably, the reconstruction of SCAN is substantially faster than ePIE. Additionally, the SCAN method appears adept at mitigating periodic artifacts, even under conditions of minimal overlap.

5. CONCLUSIONS

We have introduced SCAN, a coordinate-based neural network framework devised to advance the precision and efficiency of Fourier phase retrieval problems. Through comprehensive experimental results and ablation studies, SCAN demonstrated its robustness, especially in challenging noisy scenarios, outperforming existing methodologies. The unified network architecture and newly introduced loss function provide distinct advantages over traditionally employed unsupervised models in the domain. Extending SCAN to address broader phase retrieval challenges and applications in 3D Bragg Ptychography remains a promising avenue for future exploration.

6. REFERENCES

- [1] I. A. Vartanyants and I. K. Robinson, “Partial coherence effects on the imaging of small crystals using coherent x-ray diffraction,” *J. Condens. Matter Phys.*, vol. 13, no. 47, pp. 10593–10611, 2001.
- [2] M. Hayes, “The reconstruction of a multidimensional sequence from the phase or magnitude of its fourier transform,” *IEEE Trans. Signal Process.*, vol. 30, no. 2, pp. 140–154, 1982.
- [3] Z. Guan, E. H. R. Tsai, X. Huang, K. G. Yager, and H. Qin, “PtychoNet: Fast and high quality phase retrieval for ptychography,” in *BMVC*, 2019, pp. 222.1–222.13.
- [4] R. Manekar, K. Tayal, V. Kumar, and J. Sun, “End to end learning for phase retrieval,” in *ICML Workshop ML Interpret. Sci. Discov.*, 2020.
- [5] R. W. Gerchberg and W. O. Saxton, “A practical algorithm for the determination of the phase from image and diffraction plane pictures,” *Optik*, vol. 35, no. 2, pp. 237–246, 1972.
- [6] H. H. Bauschke, P. L. Combettes, and D. R. Luke, “Phase retrieval, error reduction algorithm, and Fienup variants: A view from convex optimization,” *J. Opt. Soc. Am. A*, vol. 19, no. 7, pp. 1334–1345, 2002.
- [7] J. R. Fienup, “Phase retrieval algorithms: A comparison,” *Appl. Opt.*, vol. 21, no. 15, pp. 2758–2769, 1982.
- [8] E. Cha, C. Lee, M. Jang, and J. C. Ye, “DeepPhaseCut: Deep relaxation in phase for unsupervised Fourier phase retrieval,” *IEEE Trans. Pattern Anal. Mach. Intell.*, vol. 44, no. 12, pp. 9931–9943, 2022.
- [9] C.-C. Chen, J. Miao, C. W. Wang, and T. K. Lee, “Application of optimization technique to noncrystalline x-ray diffraction microscopy: Guided hybrid input-output method,” *Phys. Rev. B*, vol. 76, no. 6, 2007.
- [10] M. J. Cherukara, Y. S. G. Nashed, and R. J. Harder, “Real-time coherent diffraction inversion using deep generative networks,” *Sci. Rep.*, vol. 8, no. 1, 2018.
- [11] Q. Ye, L.-W. Wang, and D. P. K. Lun, “SiSPRNet: end-to-end learning for single-shot phase retrieval,” *Opt. Express*, vol. 30, no. 18, pp. 31937–31958, 2022.
- [12] L. Wu, P. Juhas, S. Yoo, and I. Robinson, “Complex imaging of phase domains by deep neural networks,” *IUCrJ*, vol. 8, no. 1, pp. 12–21, 2021.
- [13] A. Scheinker and R. Pokharel, “Adaptive 3d convolutional neural network-based reconstruction method for 3d coherent diffraction imaging,” *J. Appl. Phys.*, vol. 128, no. 18, 2020.
- [14] Y. Yao, H. Chan, S. Sankaranarayanan, P. Balaprakash, and R. J. Harder et al., “AutophaseNN: unsupervised physics-aware deep learning of 3d nanoscale bragg coherent diffraction imaging,” *npj Comput. Mater.*, vol. 8, no. 1, 2022.
- [15] L. Wu, S. Yoo, A. F. Suzana, T. A. Assefa, and J. Diao et al., “Three-dimensional coherent x-ray diffraction imaging via deep convolutional neural networks,” *npj Comput. Mater.*, vol. 7, no. 1, 2021.
- [16] Z. Zhuang, D. Yang, F. Hofmann, D. Barmherzig, and J. Sun, “Practical phase retrieval using double deep image priors,” *Electron. Imag.*, vol. 35, no. 14, pp. 153–1–153–6, 2023.
- [17] C. A. Metzler, P. Schniter, A. Veeraraghavan, and R. G. Baraniuk, “prdeep: Robust phase retrieval with a flexible deep network,” in *ICML*, 2018, pp. 3501–3510.
- [18] P. Hand, O. Leong, and V. Voroninski, “Phase retrieval under a generative prior,” in *NeurIPS*, 2018, pp. 9154–9164.
- [19] B. Mildenhall, P. P. Srinivasan, M. Tancik, J. T. Barron, and R. Ramamoorthi et al., “NeRF: Representing scenes as neural radiance fields for view synthesis,” in *ECCV*, 2020, pp. 99–106.
- [20] V. Sitzmann, J. N. P. Martel, A. W. Bergman, D. B. Lindell, and G. Wetzstein, “Implicit neural representations with periodic activation functions,” in *NeurIPS*, 2020, pp. 7462–7473.
- [21] V. Saragadam, D. LeJeune, J. Tan, G. Balakrishnan, and A. Veeraraghavan et al., “Wire: Wavelet implicit neural representations,” in *CVPR*, 2023, pp. 18507–18516.
- [22] R. Chabra, J. E. Lenssen, E. Ilg, T. Schmidt, and J. Straub et al., “Deep local shapes: Learning local sdf priors for detailed 3d reconstruction,” in *ECCV*, 2020, pp. 608–625.
- [23] J. Chibane, A. Mir, and G. Pons-Moll, “Neural unsigned distance fields for implicit function learning,” in *NeurIPS*, 2020, pp. 21638–21652.
- [24] Y. Sun, J. Liu, M. Xie, B. Wohlberg, and U. S. Kamilov, “Coil: Coordinate-based internal learning for tomographic imaging,” *IEEE Trans. Comput. Imaging*, vol. 7, pp. 1400–1412, 2021.
- [25] J. Liu, M. M. Balaji, C. A. Metzler, M. S. Asif, and P. Rangarajan, “Solving inverse problems using self-supervised deep neural nets,” in *OSA Imaging and Applied Optics Congress 2021 (3D, COSI, DH, ISA, pcAOP)*, 2021.
- [26] H. Zhou, B. Y. Feng, H. Guo, S. Lin, and M. Liang et al., “Fourier ptychographic microscopy image stack reconstruction using implicit neural representations,” *Optica*, vol. 10, no. 12, pp. 1679–1687, 2023.
- [27] S. Xie, H. Zhu, Z. Liu, Q. Zhang, and Y. Zhou et al., “DINER: Disorder-invariant implicit neural representation,” in *CVPR*, 2023, pp. 6143–6152.
- [28] H. Zhu, Z. Liu, Y. Zhou, Z. Ma, and X. Cao, “DNF: diffractive neural field for lensless microscopic imaging,” *Opt. Express*, vol. 30, no. 11, pp. 18168–18178, 2022.
- [29] S. Marchesini, H. He, H. N. Chapman, S. Noy, and M. R. Howells et al., “X-ray image reconstruction from a diffraction pattern alone,” *Phys. Rev. B*, vol. 68, no. 14, 2003.
- [30] D. Ulyanov, A. Vedaldi, and V. Lempitsky, “Deep image prior,” in *CVPR*, 2018, pp. 9446–9454.
- [31] P. Li, N. W. Phillips, S. J. Leake, M. Allain, and F. Hofmann et al., “Revealing nano-scale lattice distortions in implanted material with 3d bragg ptychography,” *Nat. Commun.*, vol. 12, no. 1, 2021.
- [32] A. Maiden and J. M. Rodenburg, “An improved ptychographical phase retrieval algorithm for diffractive imaging,” *Ultramicroscopy*, vol. 109, no. 10, pp. 1256–1262, 2009.